

An Analysis of the Effect of the Bidirectional Reflectance Distribution Function on Remote Sensing Imagery Accuracy from Small Unmanned Aircraft Systems

Brandon Stark¹, *Student Member, IEEE*, Tiebiao Zhao², *Student Member, IEEE*
and YangQuan Chen³, *Senior Member, IEEE*

Abstract—Small Unmanned Aircraft Systems (SUASs) are increasingly being utilized for remote sensing applications due to their low-cost availability and potential for the collection of high-resolution on-demand aerial imagery. However, the field is still maturing, and there remains many questions on the accuracy and the validity of the data collected. While many researchers have investigated means of improving calibrations and data collection techniques, there are other sources of error that require investigation. In this paper, two unique characteristics of SUAS remote sensing are analyzed as potential sources of error: the use of wide field-of-view (FOV) imaging sensors and solar motion during one or more data collection flights. Both of these characteristics are related to the bidirectional reflectance distribution function (BRDF), a description of light reflection as a function of illumination direction and observer viewing angles. The wide FOV of many imaging equipment creates an inherent radial variation in viewing angle, and the solar motion creates a non-static illumination source. The results of this paper indicates that these two factors have significant contributions to errors and should not be assumed to be negligible.

I. INTRODUCTION

The use of Small Unmanned Aircraft Systems (SUASs) has grown dramatically over the past decade, especially in the field of remote sensing. They can fly on-demand, collect high resolution imagery, and can tolerate many atmospheric conditions compared to satellite imagery. For many applications, they have demonstrated immediate value, providing cost-efficient mapping solutions. However, as the technology is maturing, SUASs have increasingly targeted being utilized in data analytic driven applications such as precision agriculture [1] and field-based phenotyping [2]. These applications require a sufficient level of reflectance measurements to provide usable results.

Example projects such as those found in [1] and [3] have demonstrated promising results, though there remains questions over data accuracy and repeatability. This has led to an increased interest in data accuracy improvements such as establishing an effective methodology [4], data collection optimization [5], noise cancellation [6], and calibration techniques [7]. Hyperspectral data, especially requires significant

calibration techniques [8]. However, the majority of these approaches focus on the means and methods to improve sensor calibration and accuracy. Few address other potential sources, such as those from atmospheric transmittance effects [9].

In many discussions of SUAS-based remote sensing, the reflectance model for canopy measurements is often simplified to assume a strictly nadir (or straight down) viewing angle and a static illumination source [1], [3]. However, this assumption neglects to consider the bidirectional reflectance distribution function (BRDF). The BRDF is a function of wavelength, observer azimuth, observer zenith, illumination azimuth, and illumination zenith. In the case of satellite imagery, it can be shown that the effect of BRDF is relatively uniform. A satellite image covers such a wide region in a single frame creating a uniform illumination angle and the viewing angle is narrow, which results in a uniform observer zenith viewing angle.

However, this simplification is not valid for a SUAS equipped with a image system with a wide field-of-view (FOV). As seen in Fig. 1, the viewing angle within an imaging system can drastically differ within an image, even in a strictly nadir image. In Fig. 1, although the direct illumination is parallel, the observer zenith angle (θ) varies across the field-of-view of the imaging system. In the case of aircraft pitch or roll, the variation can be even larger. Systems that utilize a gimbal system may negate aircraft pitch or roll to maintain nadir imaging, but will suffer from the wide FOV of the camera.

A two-dimensional representation of this effect can be seen in Fig. 2. In this simulated model of a flat terrain, the observer's zenith angle varies radially from the center by as much as 30° . The imaging system simulated in Fig. 2 has a 46.4° field-of-view both vertically and horizontally, matching the vertical field-of-view of a Canon S100 camera, a commonly used camera in SUAS remote sensing applications. Many other SUASs may utilize camera systems with FOVs that range between 28.75° to over 100° in wide angle systems.

As evident in Fig. 2, the zenith angle variation is too significant to be neglected in analysis. The bidirectional reflectance distribution function (BRDF) is a function that describes how light is reflected given an illumination viewing orientation and the observing viewing orientation. It is often

¹Mechatronics, Embedded Systems and Automation Lab, School of Engineering, University of California, Merced, Merced, CA, USA, bstark2@ucmerced.edu

²Mechatronics, Embedded Systems and Automation Lab, School of Engineering, University of California, Merced, Merced, CA, USA, tzhao3@ucmerced.edu

³Mechatronics, Embedded Systems and Automation Lab, School of Engineering, University of California, Merced, Merced, CA, USA, ychen53@ucmerced.edu

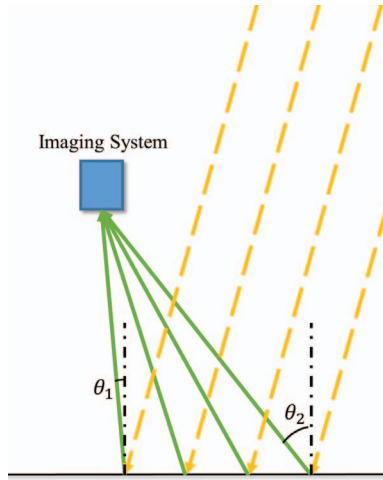


Fig. 1: Viewing angle variation within an image.

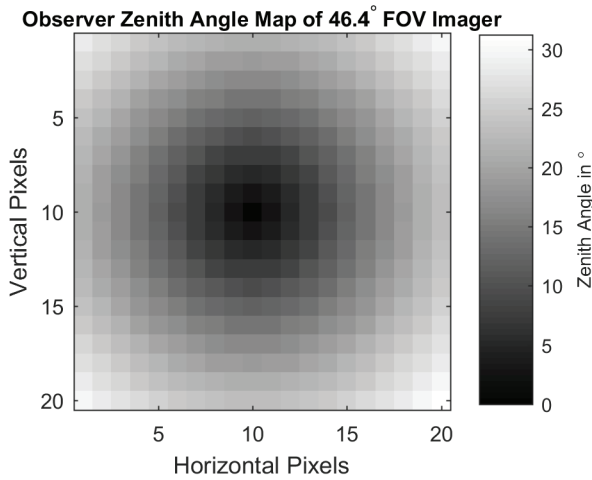


Fig. 2: The observer zenith angle varies radially from the center of the image. The degree of its variation is dependent on the imaging field-of-view.

represented as:

$$f_r(\theta_i, \phi_i; \theta_o, \phi_o; \lambda) = \frac{dL_r(\theta_o, \phi_o)}{dE(\theta_i, \phi_i)} \quad (1)$$

where the response is a function of the illumination zenith and azimuth angles (θ_i, ϕ_i) , observer zenith and azimuth angles (θ_o, ϕ_o) , and wavelength (λ) . L_r is the spectral radiance leaving the surface and E is the overall spectral irradiance.

This effect is often drastically apparent in aerial imagery in the form of hotspots or darkened corners. While vignetting effects may have a similar appearance, the wavelength dependence can be visible in multi-spectral cameras, such as in Fig. 3 in which the tree canopies in the far right side of the image are not only a different intensity, but also a different color than those on the left. Unlike vignetting effects, this radial variation may be centered anywhere in the image or out of frame.

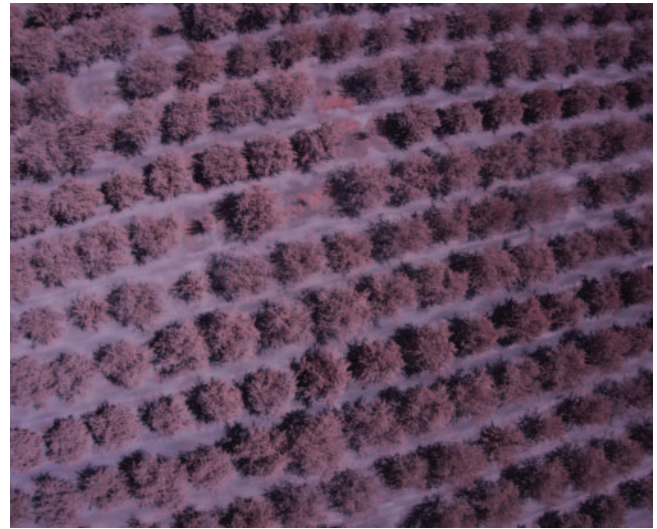


Fig. 3: The wavelength dependence on BRDF can be visually seen by the change in color of the trees from the right to the left of this image taken with a G-B-NIR modified camera (ELPH110).

The challenge of characterizing BRDF for vegetation has drawn increased interest with the growth in high resolution remote sensing data sets. SUASs have recently been investigated as a novel platform as a goniometer, a device to measure the reflected light at precise angular positions to characterize BRDFs [10]. Other methods have derived mathematical models of BRDF based on models or empirical measurements and have been employed in vegetation canopy radiative transfer models (RTMs) to simulate hyperspectral reflectances [11].

In this paper, the effect of BRDF is analyzed through a vegetation canopy RTM from the perspective of two unique characteristics of a SUAS in a remote sensing application: wide FOV and data collection duration. As SUASs often fly at low altitudes and are expected to cover significant areas, they are commonly equipped with cameras with wide FOVs ($45^\circ - 70^\circ$) and may fly as long as an hour, in which the sun location may move significantly. It is shown in simulation that both of these effects play significant roles in data accuracy and may result in poor analysis without proper calibration.

The rest of the paper is organized as follows. Section II introduces the SUAS Remote Sensing Model used to simulate the effects of BRDF of a simulated environment and imaging sensor. The methodology of the simulation analysis is presented in Section III. In Section IV, the results of the simulation sets are described. Finally, concluding remarks are presented in Section VI.

II. SUAS REMOTE SENSING MODEL

In order to effectively isolate the specific effects of BRDF introduced by the two factors, a SUAS remote sensing model and simulation was developed (Fig. 4).

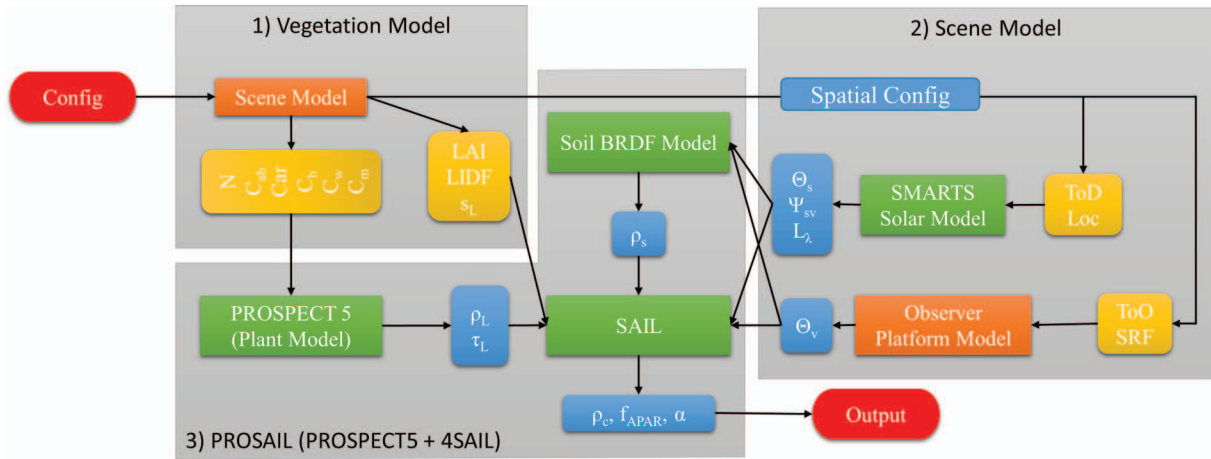


Fig. 4: SUAS Simulation Model.

A. Description of SUAS Remote Sensing Model

The model utilizes three established models combined and a SUAS model that enables simulation of a SUAS remote sensing data collection. At the leaf level, the PROSPECT5 model provides leaf optical properties in the form of reflectance across a wide spectrum as a function of leaf biochemistry, such as chlorophyll, water, and dry matter content [12]. This model is commonly combined with the Scattering by Arbitrary Inclined Leaves (4SAIL) canopy reflectance model to provide a simulation of both the spectral and directional variation of canopy reflectance [13]. The solar spectral irradiances and solar position are simulated with the Simple Model of the Atmospheric Radiative Transfer of Sunshine (SMARTS) [14].

The combination of PROSPECT5 and 4SAIL is commonly referred to as PROSAIL, and is frequently used for spectral sensitivity analysis as well as directional sensitivity analysis [13]. Reference [13] provides a survey of existing studies that utilize PROSAIL, as well as validation studies. In particular, [15] demonstrated that top-of-atmosphere hyperspectral radiances under multiple view angles could be accurately predicted.

In the simulation, a scene model is described as a $m \times n$ array of pixels, where each pixel can be assigned an individual vegetation model, including biochemical parameters and canopy parameters as described in [13]. A SUAS mission scene model is utilized to describe the date, time, location, altitude, and camera field-of-view. The outputs of both the vegetation model and the SUAS scene model are fed into PROSAIL and $m \times n$ hyperspectral simulations are run. The important parameters of interest fed into PROSAIL in this study are $\theta_i, \phi_i; \theta_o, \text{ and } \phi_o$ which are outputs of the SUAS and solar model.

B. Selection of Subcomponent Reflectance Models

The validity of the SUAS simulation model depends on the validity of the submodel components. At the leaf-level, PROSPECT pioneered the simulation of leaf directional-hemispherical reflectance and transmittance [13]. While the

accurate simulation of real-world environments requires measurement of biochemical content (chlorophyll, water and dry matter content, etc), it is assumed that the real-world accuracy is not a needed component for this analysis. The validity of the PROSPECT model to generate plausible hyperspectral reflectance is the only condition that is needed to be met.

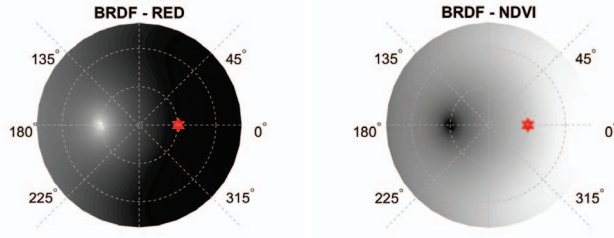
The validity of the selection of 4SAIL as a canopy reflectance model is dependent on the following assumptions. Of canopy reflectance models, two models were investigated: SAIL and FLIGHT. SAIL, one of the earliest canopy models, simulates the BRDF of turbid medium plant canopies by solving the scattering and absorption of four upward/downward radiative fluxes [13]. Since the model does not include parameters for canopy structure, the model is more similar to a homogeneous scattering of leaves over a soil. In contrast, Forward Light Interaction Model (FLIGHT) is based on a Monte Carlo simulation of photon transport, where the foliage is represented within crowns based on structural parameters which allows for accurate modeling of scattering effects [16]. Both canopy models are well-regarded and their selection depends on the object of interest. In this study, 4SAIL was selected as the composition of each pixel more resembles the assumptions in this model given the high resolution of many SUAS aerial imagery in which individual canopies are identifiable.

C. Validation of SUAS Remote Sensing Model

The results of the model match previous published research on BRDF effects [11]. Utilizing the simulation to generate visual representations of the BRDF (Fig. 5), the significant variation of reflectance is depicted. It is noted that a variation is also depicted in the calculation of the normalized difference vegetation index (NDVI) calculated as

$$NDVI = \frac{\lambda_{800nm} - \lambda_{680nm}}{\lambda_{800nm} + \lambda_{680nm}}$$

This variation is indicative of the wavelength dependence of BRDF. While both near infrared (NIR, λ_{800nm}) and red



(a) Polar plot of BRDF at 680 nm. (b) Polar plot of BRDF of a NDVI.

Fig. 5: Visual representation of BRDF in a polar plot of observer zenith and azimuth. Sun location marked with a star at a zenith angle of 20° .

(λ_{680nm}) exhibit a ‘hotspot’ at a specific viewing orientation, the intensity of the reflectance of the red wavelengths decreases at a different rate than NIR. This effect is similarly shown in Fig. 6. In this figure, the Normalized Nadir Anisotropy Factor depicts the variation in normalized scale factor across the wavelengths for a different azimuth viewing angle calculated as

$$ANIF = \frac{BRDF(\theta_i, \phi_i; \theta_{20^\circ}, \phi_{AZM}; \lambda)}{BRDF(\theta_i, \phi_i; \theta_{nadir}, \phi_0; \lambda)}$$

for a given illumination direction (θ_i, ϕ_i) across different viewing azimuths and wavelengths.

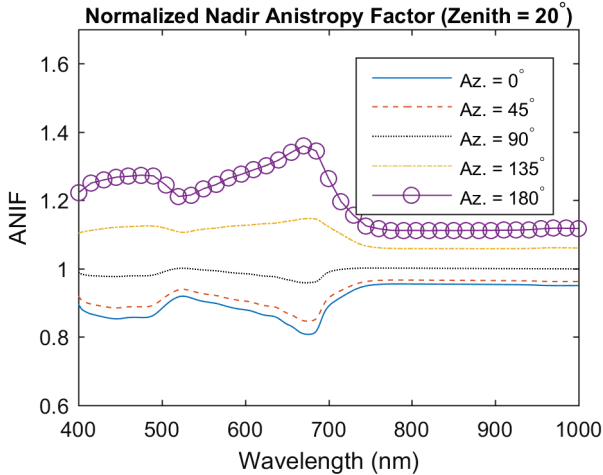


Fig. 6: Normalized Nadir Anisotropy Factor depicts the variation in normalized scale factor as a function of wavelength.

III. METHODOLOGY

In order to characterize the effect of BRDF as introduced by the unique characteristics of SUASs, two sets of analysis were conducted. First, the effect of BRDF as a result of a wide viewing angle (46.4°) was analyzed by a set of simulations of a single image. The second analysis was conducted over a series of images taken over a specified time period. In both sets of analysis, several assumptions

and simplifications were made to isolate the parameter of interest.

In all images, the terrain was assumed to be perfectly flat and that any variation in viewing angle is due to the imaging equipment field-of-view. In practice, this assumes a perfect radial correction and a perfect lens imperfection correction. The resulting hyperspectral measurements are assumed to be accurate top-of-canopy measurements, neglecting any atmospheric affects or sensor inaccuracies. The measurements are also assumed to be accurate absolutely, assuming a perfectly calibrated sensor. The top-of-canopy measurement is assumed from a static solar spectrum irradiance, irrespective of the time of the day or day of year. In the second set of simulations, this ensures that the only parameter change over the series of the image is the change in location of the sun. As an added source of variation, each image is assumed to be subject to minor variations in aircraft pitch and roll ($\mu = 0^\circ, \sigma = 2.25^\circ$) to simulate a typical SUAS flight.

In this study, two biophysical variables within the vegetation analysis are used to introduce variability of the hyperspectral response: Chlorophyll Content (C_{ab}) and Leaf Area Index (LAI). While many factors may be used, C_{ab} and LAI are among the most common variables analyzed with the PROSAIL vegetation model used [13]. Since the goal of the study is evaluate the effect of BRDF as a function of imaging FOV and sun motion, the accuracy of the variables to a real-world system is unnecessary, only that the variables are plausible. As a comparison, each simulated aerial image is compared to a simulated satellite image, which assumes a zenith angle of 0° .

To study the effect of a wide FOV, four sets of simulations were developed: Flat, C_{ab} , LAI and C_{ab} +LAI. In the Flat simulation, the region simulated is considered perfectly homogeneous with static parameters. In the C_{ab} simulation set, the chlorophyll content is randomly distributed at $35 \mu g/cm^2$ and a variance of $4 \mu g/cm^2$. The LAI simulation set contains a normal distribution of the leaf area index (LAI) centered at 3 with a variance of 0.5. The final simulation set contains a combination of both variation in both parameters.

To study the effect of a prolonged flight or multiple flights within a data collection mission, each of the four sets of simulations were run again with three time intervals: All Day (30-minute intervals), Morning (8:00 am - 8:30 am, 2 minute intervals) and Afternoon (12:30-1pm, 2 minute intervals).

IV. RESULTS

The results of the simulations show a significant impact of the BRDF introduced by the wide FOV and duration of flight.

A. Analysis of Wide FOV

The effect of a wide FOV from a typical SUAS imaging payload can be readily seen in the analysis in the variation in reflectance and NDVI in the four simulation sets. Fig. 7 depicts the spatial variation at 680 nm, 800 nm, and the resulting NDVI. In the resulting simulated image, the NDVI varies by as much as 10%, with an apparent cold spot in

Simulated Images with a 46.4° FOV Imager

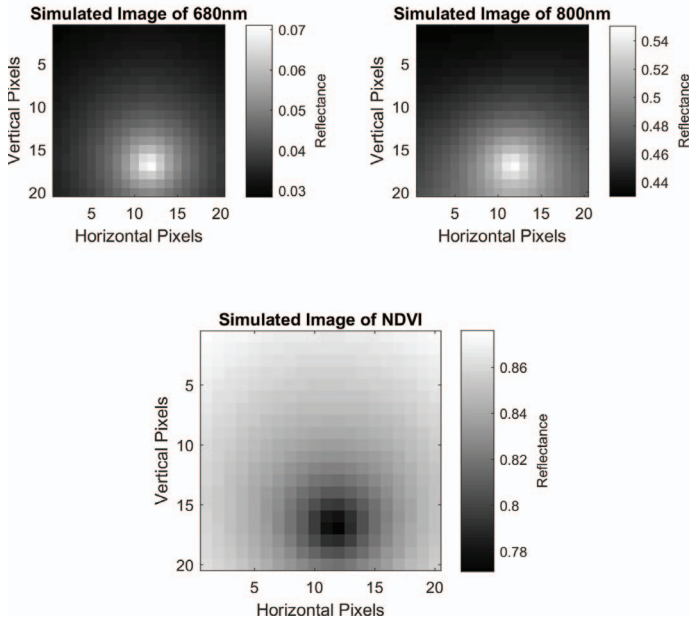


Fig. 7: Simulated Aerial Image highlighting the effect of camera FOV.

TABLE I: The variation of NDVI in the simulation sets due to wide FOV.

Image					
Sim	Min	Q1	Med	Q3	Max
Flat	0.7902	0.8512	0.8636	0.8725	0.8874
C_{ab}	0.7870	0.8481	0.8607	0.8702	0.8941
LAI	0.6430	0.8300	0.8588	0.8782	0.9148
C_{ab} +LAI	0.6818	0.8322	0.8590	0.8778	0.9193
Satellite					
Flat	0.8458	0.8458	0.8458	0.8458	0.8458
C_{ab}	0.8232	0.8426	0.8457	0.8479	0.8528
LAI	0.6558	0.8204	0.8443	0.8621	0.9001
C_{ab} +LAI	0.6573	0.8238	0.8451	0.8636	0.9074

NDVI occurring at the ‘hotspot’ or antisolar point at 680 nm and 800 nm. The wavelength variation in BRDF manifests in this NDVI variation as previously seen in Fig 5. It is important to note that the cold spot seen in Fig. 7 does not align with the zenith angle map used in the simulation, seen in Fig. 2. In this case, simply utilizing vignetting corrections to correct the resulting NDVI is improper.

The variation in reflectance is more pronounced in the other data sets. Table I depicts the variation in NDVI, as described using a Five-Number-Summary to describe the asymmetric spread: Min, 1st Quantile (Q1), Median, 3rd Quantile (Q3), and Max. It is evident that the introduction of imager FOV results in a different distribution in calculations.

Figs. 8-10 depict the relationship between the simulated satellite imagery and simulated aerial imagery of the resulting calculation of NDVI. While the impact of BRDF from a wide FOV did not significantly change the resulting

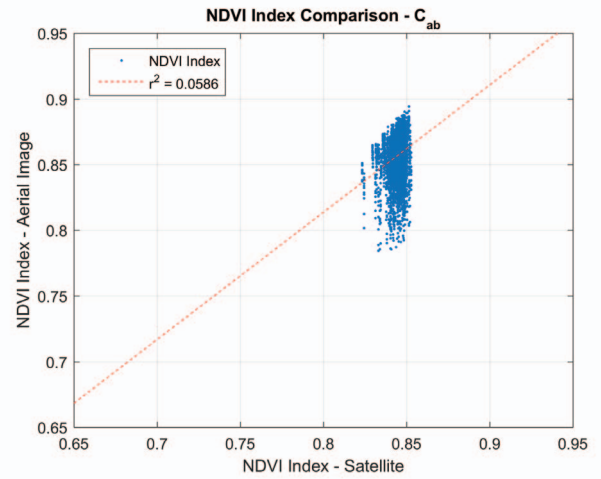


Fig. 8: When C_{ab} is varied, the source of error introduced by the wide FOV obscures the relationship with NDVI.

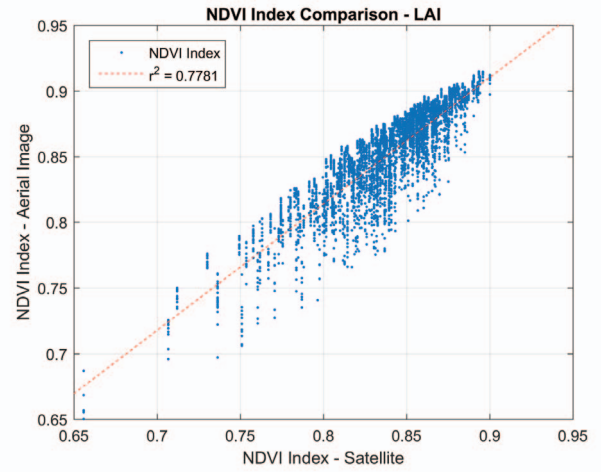


Fig. 9: NDVI is more sensitive to changes in LAI and the wide FOV does not obscure the relationship.

NDVI relationship as seen in Figs. 9 and 10, it introduced significant variability and error. Fig. 8 depicts a significantly poorer performance, this may be attributed to the insensitive relationship between chlorophyll content and resulting NDVI as described in literature [11].

The impact of BRDF from a wide FOV can be more readily apparent when using NDVI with parameter inversion to predict biochemical properties. Figs. 11, 12, and 13 depict the relationships between the C_{ab} , LAI and NDVI. As expected, the simulated satellite image depicts well-defined relationships, suitable for inversion. However, the simulated aerial imagery is much less defined though the relationship is coherent enough to be recognizable. In the case of LAI in the simulation set C_{ab} +LAI, the R^2 goodness of fit reduces from 0.9864 to 0.7476 in the presence of BRDF effects introduced by a wide FOV.

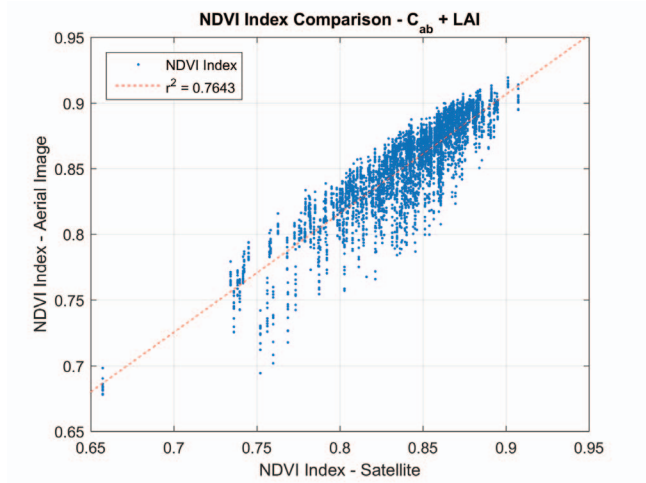


Fig. 10: The sensitivity of NDVI to changes in LAI masks the relationship with C_{ab} , however the introduction of error from a wide FOV is still significant.

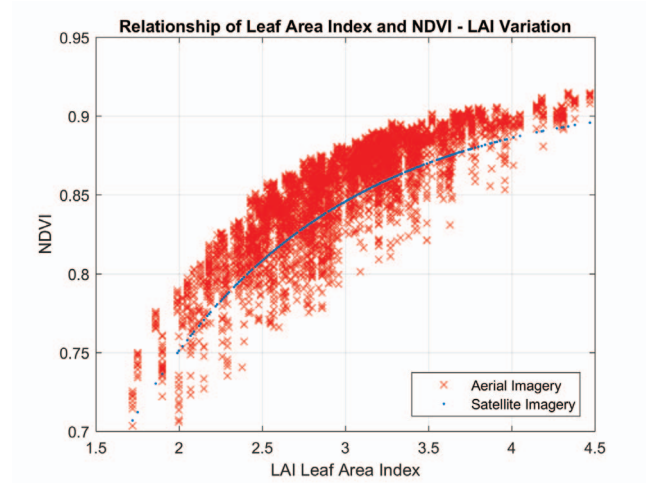


Fig. 12: The relationship between LAI and NDVI is recognizable in the presence of a wide FOV, but with a noticeable loss of accuracy.

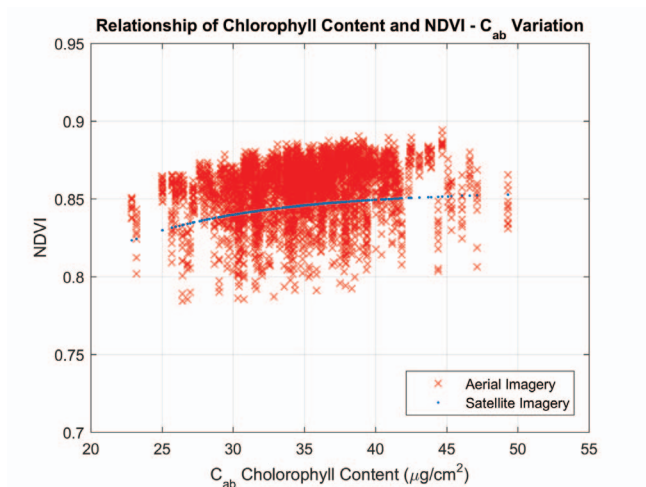


Fig. 11: The relationship between chlorophyll content and NDVI is easily obscured by the error introduced from a wide FOV.

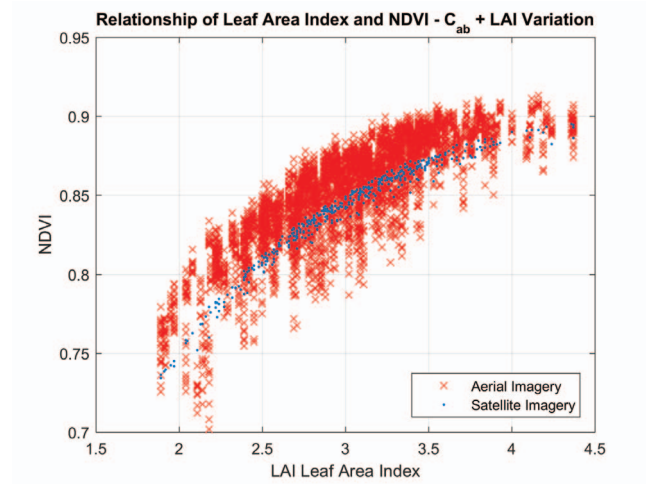


Fig. 13: The addition of a second variable (C_{ab}) minorly reduced inversion accuracy, but not to the degree that the wide FOV introduced.

B. Analysis of Solar Motion

The effect of the solar motion during a SUAS flight or mission is shown to be significant. Across a whole day, the NDVI varies significantly as a function of the solar position. The set of four full-day simulations can be seen in Figs. 14-17. In all four simulations, the NDVI varied from a maximum mean and minimal variance in the late afternoon to a minimum mean with a maximal variance around noon. The boxplots depicts the distribution with a spread as much 25%. The added effect of the wide FOV is apparent in a comparison of the simulated aerial imagery and the simulated satellite imagery.

The variance throughout the day is significant and unrelated to solar intensity or albedo. The variation in reflectance is a function of solar illumination direction, as the solar

irradiance and intensity was kept constant for the simulation sets. The result of this depicts that solar motion plays a significant role in data accuracy and should not be neglected.

The effect of solar motion is not uniform across wavelengths and is not uniform within an image due to the imagers FOV as seen in Fig. 18. Fig. 18 depicts the variation of NDVI derived from simulated aerial imagery normalized by NDVI derived from satellite imagery. While the mean largely stays close to 1, the resulting analysis depicts a time dependence that corresponds to the appearance of the hotspot in the simulated imagery. The results from these simulations indicate that it is unsuitable to directly compare imagery from one time-span to another time-span without correction for both solar motion and image FOV.

The effect of solar motion significantly affects the accuracy of parameter inversion as well. Figs. 19 and 20

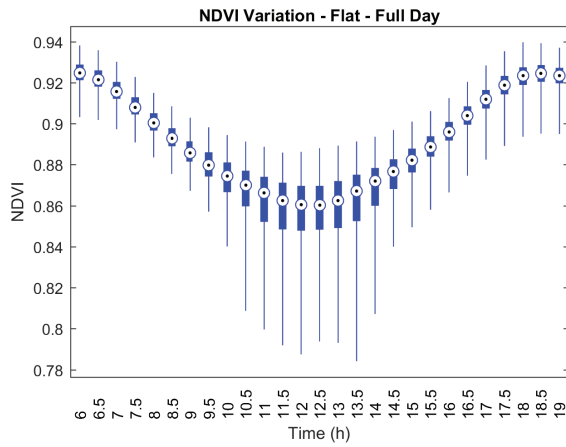


Fig. 14: The variation is minimal throughout most of the day, until the sun reaches its apex around noon.

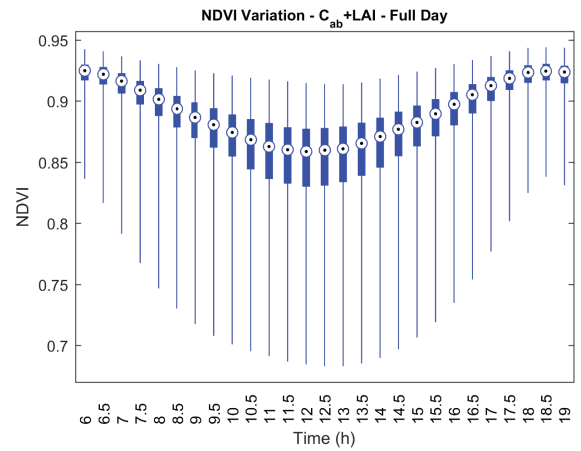


Fig. 17: The combination of both C_{ab} and LAI with solar motion and image FOV introduces a significant variance in NDVI.

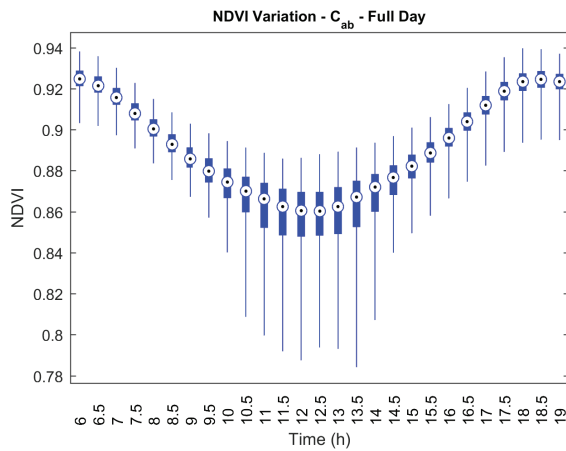


Fig. 15: Variations in C_{ab} has a minimal effect on NDVI but a similar dependence on solar motion is apparent.

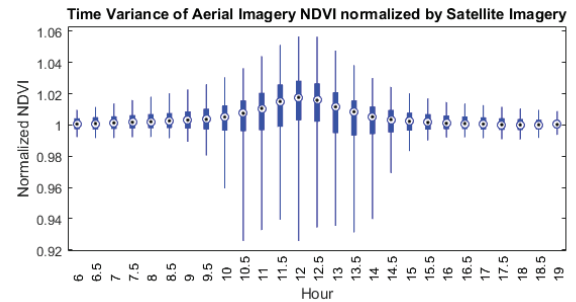


Fig. 18: The variance in NDVI due to solar motion is amplified by the effect of BRDF from wide FOV and is apparent with insufficient uniform correction.

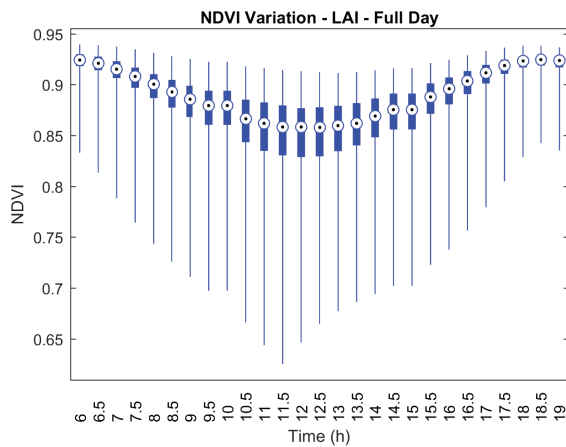


Fig. 16: Variation in LAI has a larger effect on NDVI, but the time variance due to solar motion is clear.

depict the relationship of chlorophyll and LAI respectively over the course of an entire day. As expected, the inversion of chlorophyll directly from NDVI is unfeasible given the variation in solar motion, even from the simulated satellite imagery. The inversion of leaf area index suffers from poor performance, though the time variation from solar motion can be seen in the patterns of the relationship.

The results from the simulation over the course of an entire day depict the severe role that solar motion plays on remote sensing measurements. Special care should be taken when collecting aerial imagery over the course of an entire day, as is common when using a SUAS over a large area. Comparisons across time-periods, even with accurate spectral sensor measurements, is subject to errors introduced by BRDF at top-of-canopy measurements.

In the final set of simulations, the variation in reflectance is evaluated within a 30-minute window, such as would be common in a short SUAS flight.

While the variation in solar motion is significant over the course of an entire day, the variation is nearly unnoticeable at both morning and afternoon windows. Figs. 22 and 21 depict

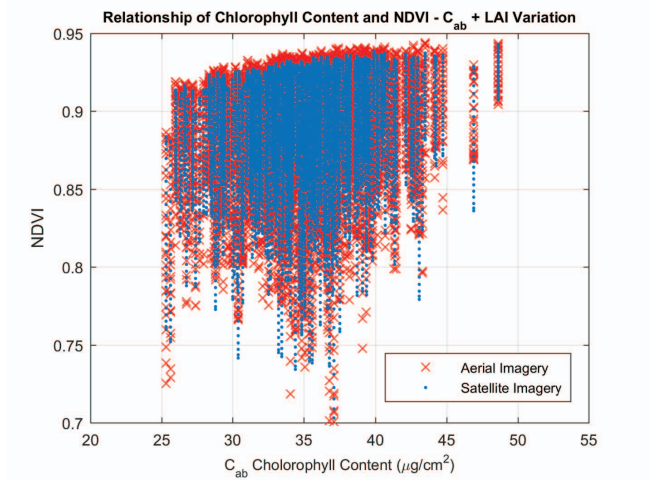


Fig. 19: The relationship between C_{ab} and NDVI is obscured by noise from wide FOV and solar motion.

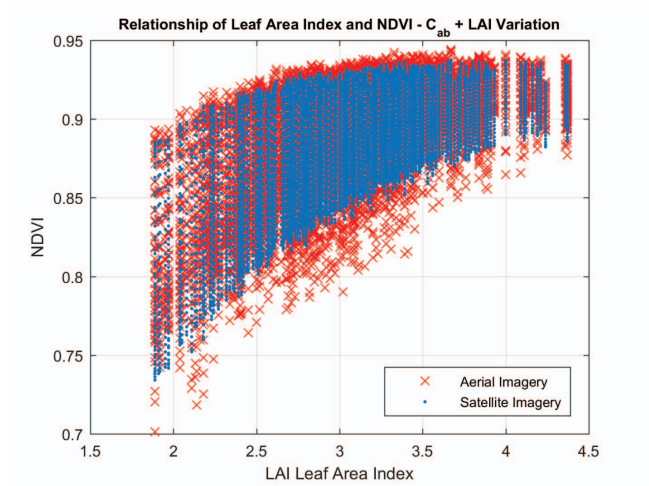


Fig. 20: The relationship between LAI and NDVI is visible, but the effect of solar motion introduces error in both simulated satellite and aerial imagery.

the variation within the images during their time windows, from the simulations with variance in both C_{ab} and LAI. The stability of the NDVI measurements indicate that with a static solar intensity, the solar motion does not play a significant role in data errors.

While the boxplot depicts a stable response of NDVI during a 30-minute time-window, a closeup of the relationship of simulated satellite imagery and simulated aerial imagery depicts the variance and clear time dependence of reflectance measurements 23. Within a short time-window, these patterns may not play a significant role, but may become significant in larger time-windows.

V. CONCLUSION

The field of remote sensing with small unmanned aerial systems is starting to grow, however, there remains significant questions over the accuracy and validity of the data

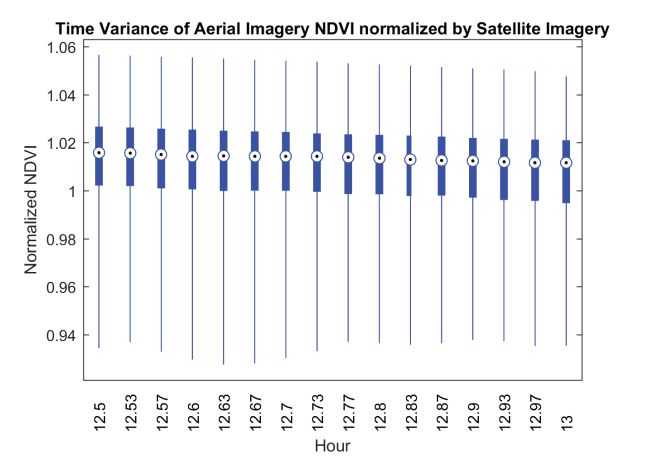


Fig. 21: Boxplot of NDVI variance in the afternoon (12:30pm to 1:00pm).

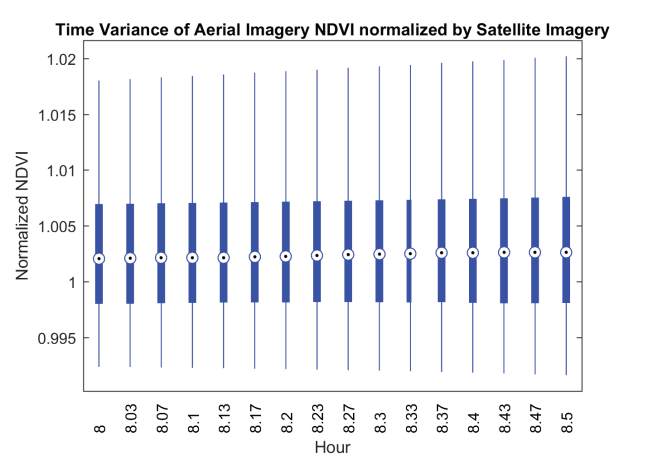


Fig. 22: Boxplot of NDVI variance in the morning (8:00am to 8:30am).

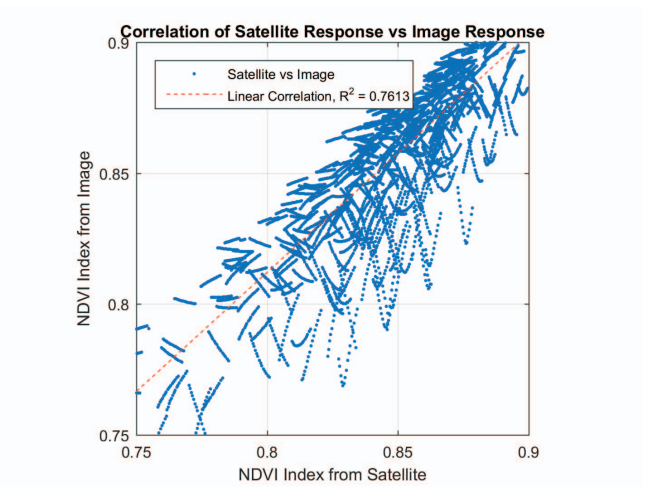


Fig. 23: Normalized Nadir Anistropy Factor depicts the variation in normalized scale factor as a function of wavelength.

generated. SUASs can provide significant advantages over traditional satellite imagery, however, the validity of the data must be assessed. In this paper, a comprehensive set of simulations was developed to analyze the effect of two characteristics unique to low-altitude SUASs: the use of wide angle field-of-view cameras used to enable adequate area coverage and the solar motion during a flight or multiple flights.

The results in these simulations indicate that these two factors are sources of inaccuracies and may not be adequately compensated for in many SUAS remote sensing workflows. While these are not the only potential sources of error, these represent inherent sources of errors which are not associated with sensor technology or data processing. As such, these may prove to be more difficult to overcome as it challenges the existing methodology. Adjustments to data collections may include deploying multiple vehicles simultaneously during a short time interval and narrowing the imaging FOV. This may reduce errors to within an acceptable tolerance, albeit at a significantly higher cost.

REFERENCES

- [1] J. A. Berni, P. J. Zarco-Tejada, L. Suárez, and E. Fereres, "Thermal and narrowband multispectral remote sensing for vegetation monitoring from an unmanned aerial vehicle," *Geoscience and Remote Sensing, IEEE Transactions on*, vol. 47, no. 3, pp. 722–738, 2009.
- [2] S. C. Chapman, T. Merz, A. Chan, P. Jackway, S. Hrabar, M. F. Dreccer, E. Holland, B. Zheng, T. J. Ling, and J. Jimenez-Berni, "Pheno-copter: a low-altitude, autonomous remote-sensing robotic helicopter for high-throughput field-based phenotyping," *Agronomy*, vol. 4, no. 2, pp. 279–301, 2014.
- [3] T. Zhao, B. Stark, Y. Chen, A. L. Ray, and D. Doll, "A detailed field study of direct correlations between ground truth crop water stress and normalized difference vegetation index (NDVI) from small unmanned aerial system (sUAS)," in *Unmanned Aircraft Systems (ICUAS), 2015 International Conference on*, pp. 520–525, IEEE, 2015.
- [4] B. Stark and Y. Q. Chen, "Remote Sensing Methodology for Unmanned Aerial Systems," in *Encyclopedia of Aerospace Engineering - UAS* (R. Blockley and W. Shyy, eds.), Wiley, 2016.
- [5] B. Stark and Y. Chen, "Optimal Collection of High Resolution Aerial Imagery with Unmanned Aerial Systems," in *Unmanned Aircraft Systems (ICUAS), 2014 International Conference on*, pp. 89–94, IEEE, 2014.
- [6] J. Kelcey and A. Lucieer, "Sensor correction of a 6-band multispectral imaging sensor for UAV remote sensing," *Remote Sensing*, vol. 4, no. 5, pp. 1462–1493, 2012.
- [7] E. Salami, C. Barrado, and E. Pastor, "UAV flight experiments applied to the remote sensing of vegetated areas," *Remote Sensing*, vol. 6, no. 11, pp. 11051–11081, 2014.
- [8] E. Honkavaara, H. Saari, J. Kaivosoja, I. Pölönen, T. Hakala, P. Litkey, J. Mäkynen, and L. Pesonen, "Processing and assessment of spectrometric, stereoscopic imagery collected using a lightweight UAV spectral camera for precision agriculture," *Remote Sensing*, vol. 5, no. 10, pp. 5006–5039, 2013.
- [9] M. T. Chyliński and M. Ostrowski, "Error simulations of uncorrected NDVI and DCVI during remote sensing measurements from UAS," *Miscellanea Geographica*, vol. 18, no. 2, pp. 35–45, 2014.
- [10] A. Burkart, H. Aasen, L. Alonso, G. Menz, G. Bareth, and U. Rascher, "Angular dependency of hyperspectral measurements over wheat characterized by a novel UAV based goniometer," *Remote sensing*, vol. 7, no. 1, pp. 725–746, 2015.
- [11] H. G. Jones and R. A. Vaughan, *Remote Sensing of Vegetation*. Oxford University Press, New York, USA, 2010.
- [12] J.-B. Feret, C. François, G. P. Asner, A. A. Gitelson, R. E. Martin, L. P. Bidel, S. L. Ustin, G. le Maire, and S. Jacquemoud, "PROSPECT-4 and 5: Advances in the leaf optical properties model separating photosynthetic pigments," *Remote Sensing of Environment*, vol. 112, no. 6, pp. 3030–3043, 2008.
- [13] S. Jacquemoud, W. Verhoef, F. Baret, C. Bacour, P. J. Zarco-Tejada, G. P. Asner, C. François, and S. L. Ustin, "PROSPECT+ SAIL models: A review of use for vegetation characterization," *Remote Sensing of Environment*, vol. 113, pp. S56–S66, 2009.
- [14] C. A. Gueymard, "Parameterized transmittance model for direct beam and circumsolar spectral irradiance," *Solar Energy*, vol. 71, no. 5, pp. 325–346, 2001.
- [15] J. Verrelst, M. E. Schaepman, B. Koetz, and M. Kneubühler, "Angular sensitivity analysis of vegetation indices derived from CHRIS/PROBA data," *Remote Sensing of Environment*, vol. 112, no. 5, pp. 2341–2353, 2008.
- [16] P. R. North, "Three-dimensional forest light interaction model using a Monte Carlo method," *Geoscience and Remote Sensing, IEEE Transactions on*, vol. 34, no. 4, pp. 946–956, 1996.